1 *Article*

A Reversible Protonic Ceramic Cell with Symmetrically Designed Pr$_2$NiO$_{4+\delta}$-Based Electrodes: Fabrication and Electrochemical Features

Artem Tarutin [1,2], Julia Lyagaeva [1,2], Andrey Farlenkov [1,2], Sergey Plaksin [1], Gennady Vdovin [1], Anatoly Demin [1,2], and Dmitry Medvedev [1,2,*]

[1] Institute of High Temperature Electrochemistry, Yekaterinburg 620137, Russia
[2] Ural Federal University, Yekaterinburg 620002, Russia
* Correspondence: dmitrymedv@mail.ru; Tel.: +7-343-3623202

Abstract: Reversible protonic ceramic cells (rPCCs) combine two different operation regimes, fuel and electrolysis modes, which allow reversible chemical-to-electrical energy conversion at reduced temperatures with high efficiency and performance. Here we present novel technological and materials science approaches, enabling a rPCC with symmetrical functional electrodes to be prepared using a single sintering step. The response of the cell fabricated on the basis of P–N–BCZD|BCZD|PBN–BCZD (where BCZD = BaCe$_{0.5}$Zr$_{0.3}$Dy$_{0.2}$O$_{3-\delta}$, PBN = Pr$_{1.9}$Ba$_{0.1}$NiO$_{4+\delta}$, P = Pr$_2$O$_3$, N = Ni) is studied at different temperatures and water vapor partial pressures by means of volt-ampere measurements, electrochemical impedance spectroscopy and distribution of relaxation times analyses. The obtained results demonstrate that symmetrical electrodes exhibit classical mixed-ionic/electronic conducting behavior with no hydration capability at 750 °C; therefore, increasing the pH$_2$O values in both reducing and oxidizing atmospheres leads to some deterioration of their electrochemical activity. At the same time, the electrolytic properties of the BCZD membrane are improved, positively affecting the rPCC's efficiency. The electrolysis mode of the rPCC is found to be more efficient than the fuel cell mode under highly humidified atmospheres, since its performance is determined by the ohmic resistance, which decreases under respectively less humid conditions.

Keywords: PCFCs/PCECs; Ruddlesden-Popper phases; symmetrical cells; proton-conducting electrolytes

1. Introduction

Solid oxide systems with predominant protonic transport are considered as advanced applied materials for the energy sector. A particular interest is associated with their utilization as proton-conducting electrolytes in protonic ceramic cells (rPCCs), reversible solid oxide cells that are used to convert different types of energy with high efficiency and no harmful impact [1–5]. Compared with conventional solid oxide cells with oxygen-ionic electrolytes, rPCCs are able to operate at reduced temperatures due to their high proton mobility and low activation energy [6–8]. These advantages may feasibly lead to their commercialization in the near future [9]. Therefore, carrying out the necessary applied and fundamental research in this field, as well as developing new approaches for the optimization of the relevant technological and electrochemical processes, are among highly relevant current trends.

Recently, many efforts have been made to simplify technological processes involved in the fabrication of solid oxide devices based on oxygen-ionic or proton-conducting electrolytes [10,11]. One of these efforts consists in designing electrochemical cells having symmetrical electrodes [12] as an efficient strategy for reducing fabrication costs. Here, the economic benefit lies in minimizing not

45 only the number of functional materials used, but also the preparation steps. Moreover, this strategy
46 can help to resolve problems associated with thermal incompatibility and electrochemical
47 degradation if the latter has a reversible nature [13,14]. However, materials for symmetrical
48 electrodes preparation must satisfy certain requirements, such as excellent electrochemical activity in
49 both reduced (Red) and oxidized (Ox) conditions, as well as appropriate phase and thermal behavior
50 under RedOx cycling. As a rule, only a limited series of materials can be used for this purpose,
51 including Ti-, Fe-, Cr- and Mn-based oxides with simple or double perovskite structures [12].

52 Although the utilization of symmetrical solid oxide fuel cells based on oxygen-ionic electrolytes
53 has been intensively studied in the past few years [13–17], the application of this strategy to PCCs is
54 only at the beginning of its development. In the present work, we propose to use a $Pr_2NiO_{4+\delta}$-based
55 oxide in symmetrical functional layers for a rPCC. In contrast to the previously mentioned simple or
56 double perovskite, a layered structure of praseodymium nickelate is substituted under reducing
57 atmospheres to complete Ni reduction and formation of a Ni–Pr_2O_3 cermet (Figure 1) with good
58 electrocatalytic properties [18,19]. Along with the symmetrical electrode application and reversible
59 operation mode, a one-step sintering procedure was successfully used for the designed PCC due to
60 the close thermal expansion coefficients (TECs) of $Pr_2NiO_{4+\delta}$- and $Ba(Ce,Zr)O_3$-based materials [20,21].
61 The effectiveness of these three strategies was subsequently supported by the electrochemical results.

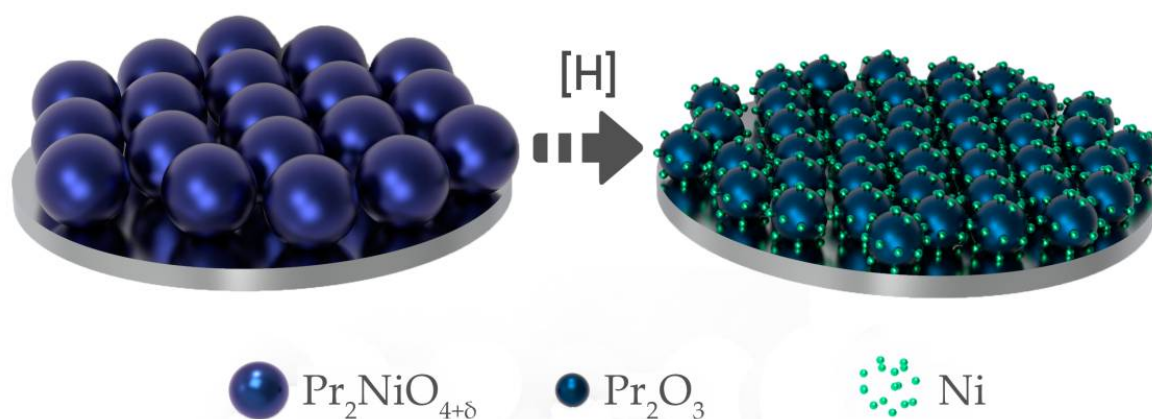62 **Figure 1.** Principal scheme of $Pr_2NiO_{4+\delta}$ reduction with the formation of a Ni-based cermet.

63 **2. Materials and Methods**

64 *2.1. Preparation of Materials*

65 The protonic ceramic cell (PCC) was fabricated from three functional materials, including
66 $BaCe_{0.5}Zr_{0.3}Dy_{0.2}O_{3-\delta}$ (BCZD) as a proton-conducting electrolyte layer (EL), its mixture with nickel
67 oxide as a substrate for supporting fuel electrode layer (SFEL) and $Pr_{1.9}Ba_{0.1}NiO_{4+\delta}$ (PBN) as a basis
68 for functional oxygen (FOEL) and functional fuel (FFEL) electrode layers.

69 The BCZD and BPN powders were obtained using the citrate-nitrate synthesis method described
70 in detail in our previous works [22,23].

71 *2.2. Characterization of Materials*

72 The phase structure of the individual materials (BCZD, PBN) and their mixture (1:1 at ratio)
73 calcined at 1350 °C for 3 h was studied by X-ray diffraction analysis (Rigaku D/MAX-2200VL [24]).
74 The scans were performed under $CuK_{\alpha 1}$ radiation between 20° and 80° with a scan step of 0.02° and
75 a scan rate of 3° min^{-1}.

76 The morphology of the ceramic samples and multilayered cell was studied using scanning
77 electron microscopy (SEM) and energy dispersive X-ray (EDX) analyses on a Tescan Mira 3 LMU
78 microscope with an Oxford Instruments INCA Energy X-MAX 80 spectrometer [24].

79 Thermogravimetric (TG) technique (Netzsch STA 449 F3 Jupiter) was employed to study
80 reduction behavior of the PBN powder.

81 Conductivity measurements were carried out in air and wet H_2 atmospheres using a convenient
82 4-probe DC current method (Zirconia-318 measurement station).

83 *2.3. Fabrication of the PCC*

84 The single-phase BCZD was mixed with NiO and starch (pore former) in a weight ratio of 3:2:1
85 to prepare the powder for the SFEL, while BCZD was mixed with PBN and pore former in a weight
86 ratio of 4:1:1 to be used as FOEL and FFEL. The mixing stages were performed using a Fritsch
87 Pulverisette 7 planetary ball mill with the following conditions: zirconia milling balls, acetone media,
88 500 rpm for 0.5 h. The corresponding powders were mixed with an organic binder (butadiene rubber
89 in acetone/benzene solvent) and rolled used a Durtson rolling mill to fabricate the functional films
90 having the required thicknesses. These films were then co-rolled with each other (tape-calendering
91 method), adjusted by ~30 μm for the raw EL, ~20 μm for the raw FOEL and FFEL and ~800 μm for
92 the raw SFEL. The green multilayered NiO–BCZD|PBN–BCZD|BCZD|PBN–BCZD structure was
93 slowly (1 °C min^{-1}) heated up to 900 °C to decompose and remove organic residue, then heated
94 further to 1350 °C at a heating rate of 5 °C min^{-1}, sintered at this temperature for 3 h and cooled to
95 room temperature at a cooling rate of 5 °C min^{-1}.

96 *2.4. Characterization of the PCC*

97 The fabricated PCC was characterized at a temperature range of 600–750 °C under reversible
98 operation (bias changes from 0.1 to 1.5 V with a step of 25 mV). The volt-ampere dependences and
99 impedance spectra were obtained using a complex of Amel 2550 potentiostat/galvanostat and
100 Materials M520 frequency response analyzer. To evaluate the electrode response, hydrogen as a fuel
101 and air as an oxidant were humidified to varying degrees. The target water vapor partial pressure
102 values were set by passing the corresponding atmospheres through a water bubbler heated to certain
103 temperatures. The impedance spectra were obtained across a frequency range of 10^{-2}–10^5 Hz at a
104 perturbation voltage of 25 mV and were then analyzed utilizing the methods of equivalent circuits
105 (Zview software) and distribution of relaxation times (DRT, DRTtools core of the Matlab software).

106 **3. Results and Discussion**

107 *3.1. $Pr_{1.9}Ba_{0.1}NiO_{4+\delta}$ Functionality*

108 To assess the applied prospect of PBN as electrodes for PCCs, its properties were
109 comprehensively studied (Figure 2).
110 This material is characterized by a high chemical compatibility with the proton-conducting
111 electrolytes based on $Ba(Ce,Zr)O_3$ (Figure 2a), since the high-temperature treatment results in
112 maintaining the basic structures for both phases, although a small amount of NiO exists at the same
113 time (this impurity phase is also visible at the interface regions, see the Ni-element distribution map
114 on Figure 3c). According to our best knowledge, we have used the highest temperature (1350 °C), at
115 which chemical interactions of cerate-zirconates and nickelates were studied. Such excellent results
116 in phase stability can be explained by the fact that $Pr_2NiO_{4+\delta}$ is doped with barium, that compensates
117 the Ba-concentration difference between two components and, therefore, diminishes a degree of
118 chemical interaction [25,26].
119 As reported in Figure 2b, the PBN material in a powder state starts to reduce at 300 °C, when
120 interstitial (and a part of lattice-site) oxygen is gradual removed [27]; this nickelate is almost
121 completely decomposed at temperatures above 600 °C, which is in line with the following simplified
122 reaction: $Pr_2NiO_{4+\delta} \rightarrow Pr_2O_3 + Ni$, see Figure 1.
123 Conductivity of the as-prepared ceramic sample in air atmosphere differs from one of the
124 reduced sample in wet hydrogen by more than 4 orders of magnitude (Figure 2d). It can be concluded
125 that the reduced sample represents a mixture of $(Pr,Ba)_2O_3$ and Ni with a mole ratio of 2:1. In other
126 words, the total conductivity is determined by oxide phases, since no continuous high conductive
127 metallic framework is formed under such a reduction. Nevertheless, Ni-particles appears during the
128 exsolution procedure (Figure 2c), which is found to be a remarkable factor in electrode processes

129   improvement [28]. According to Figure 2c, a certain part of Pr_2O_3 is transformed to $Pr(OH)_3$, but this
130   hydroxide is formed at relatively low temperatures only (under cooling of the sample in static air),
131   when Pr_2O_3 chemisorbs steam of air.
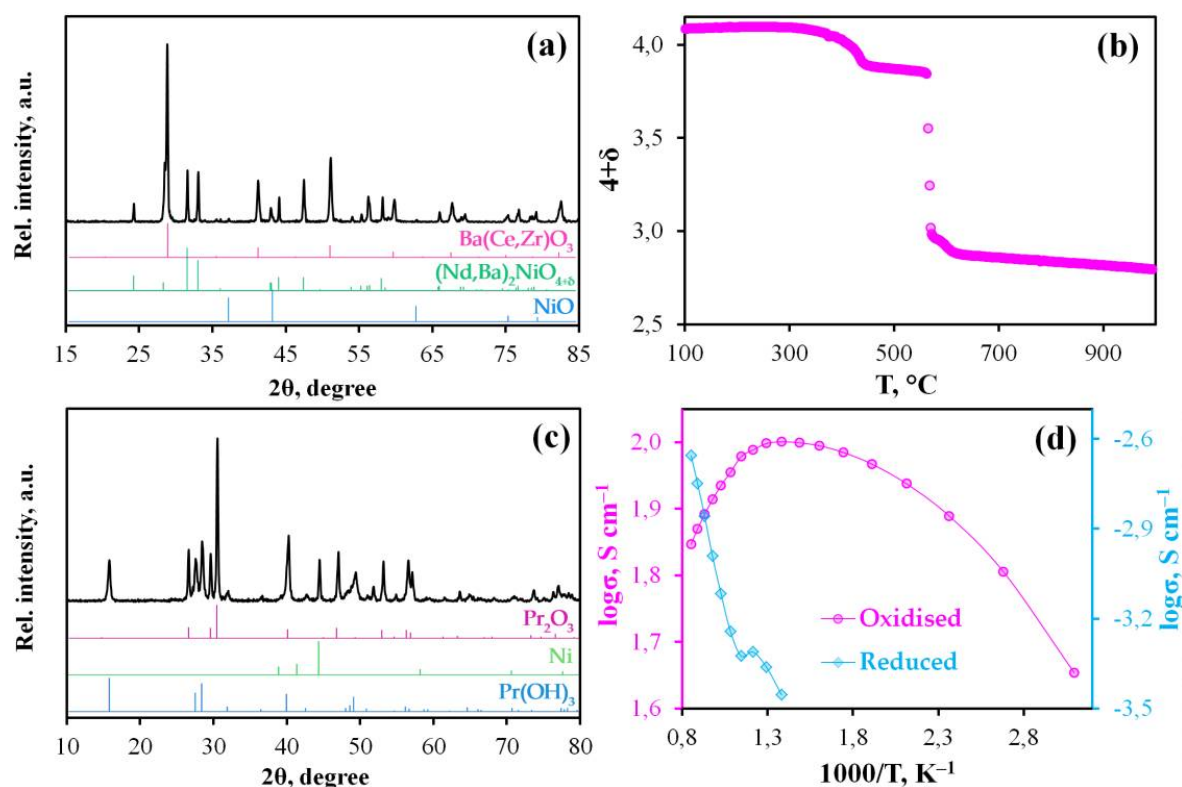132

133   **Figure 2.** (**a**) XRD pattern of the BCZD – PBN mixture calcined at 1350 °C for 5 h; (**b**) TG curve
134   obtained under reduction of the PBN powder in 50%H_2/N_2 atmosphere; (**c**) XRD pattern of the
135   reduced product of the PBN material (after TG analysis); (**d**) Conductivity of the PBN samples in
136   oxidizing and reducing atmospheres.

137   *3.2. Microstructural Features*

138   The PCC fabricated using the one-step sintering procedure shows a well-organized, multi-
139   layered structure without any visible deformation, material delamination or cracks (Figure 3a). The
140   obtained results can be explained by the excellent thermal compatibility of the $Ln_2NiO_{4+\delta}$-based
141   materials with $Ba(Ce,Zr)O_3$ proton-conducting electrolytes, especially the low chemical expansion in
142   contrast to that of many electrode materials having perovskite-related structures [29,30].
143   The resulting thickness of the FOEL, EL and FFEL are estimated to be about 15, 25 and 17 μm,
144   respectively (Figure 3b), while the total PCC thickness is equal to 700 μm. The porosity of SFEL
145   evaluated using ImageJ software amounts to 40 ± 5 vol.%; the porosity of the functional electrodes
146   does not exceed 20% (measured on the individually prepared pellets with the same composition,
147   BCZD : PBN : starch = 4:1:1), indicating their strong sintering behavior despite of 20 wt.% of pore
148   former used.
149   According to EDX analysis (Figure 3c), elements are evenly distributed and do not show
150   significant interdiffusion, forming clearly separated interphase boundaries. This also supports the
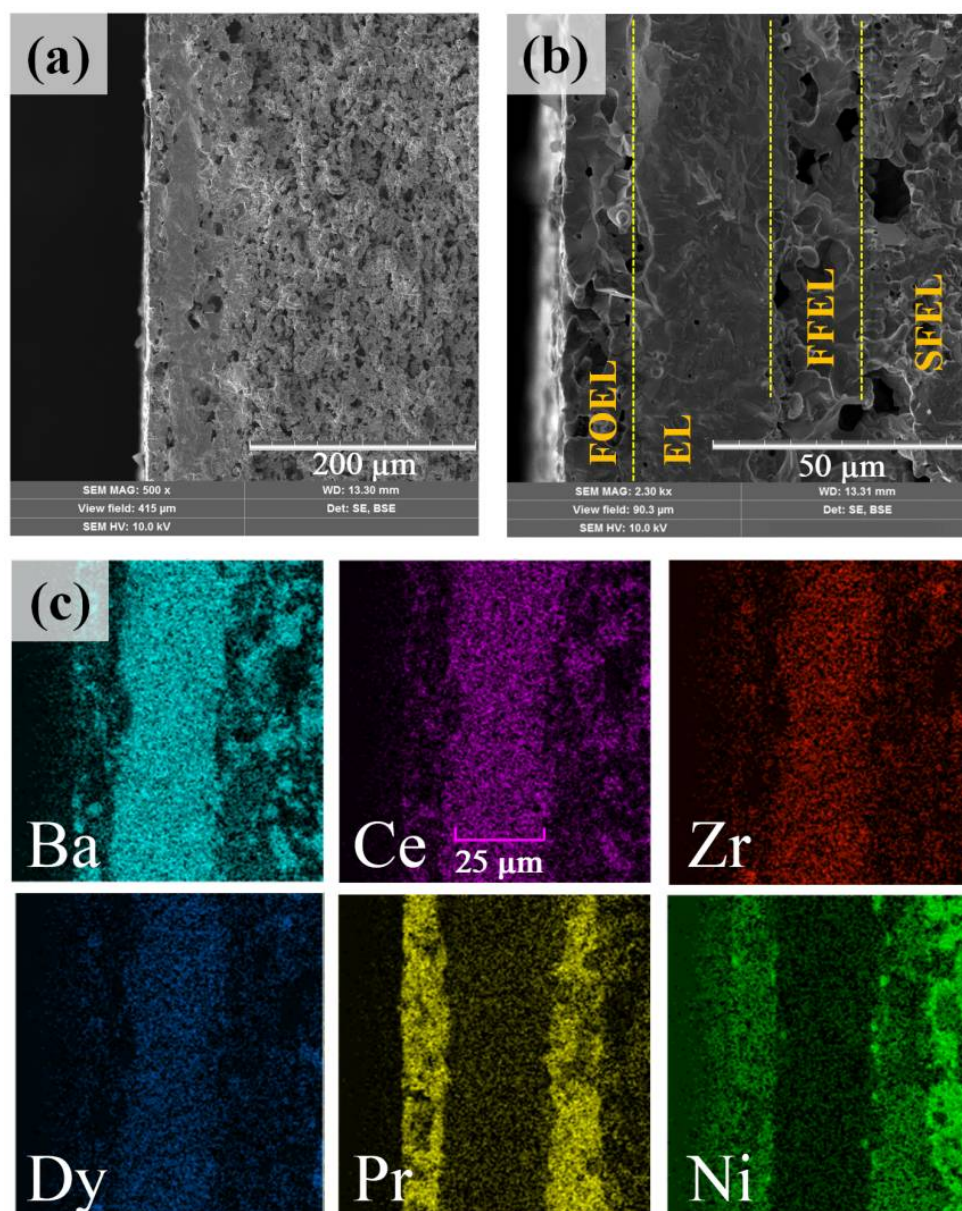151   conclusion regarding the chemical compatibility of materials used, at least at a sintering temperature
152   of 1350 °C.

Figure 3. Cross-section images of the fabricated rPCC at different magnification (**a**,**b**) and maps of the elements distribution (**c**).

3.3. Volt-Ampere Dependences and Related Properties

The operability of the reversible PCC is shown in Figure 4a. In the current-free mode, this cell generates open circuit voltages (OCV) of 1.076, 1.051, 1.006 and 0.979 V at 600, 650, 700 and 750 °C, respectively. These values are somewhat lower than those theoretically predicted, which amount to 1.135, 1.126, 1.118 and 1.109 V, respectively. Since this cell maintains gas-impenetrability (measured at room temperature under 10^{-3} atm/1 atm of total gas pressures gradient), the most likely reason for the observed differences is non-ionic conduction of the BCZD electrolyte. Indeed, both $BaCeO_3$- and $BaZrO_3$-based materials demonstrate meaningful electron conductivity in oxidizing conditions at high temperatures [31,32]. Regarding the BCZD electrolyte, its ionic transference numbers (t_i) estimated as a ratio of its ionic conductivity measured in wet H_2 to the total conductivity measured in wet air only reached 0.78, 0.62, 0.50 and 0.44 at 600, 650, 700 and 750 °C [33]. It should be noted that these t_i values were determined for the samples in system with unseparated gas space, when all the samples' sides were in contact with the same atmosphere. In the case of PCC, the electrolyte membrane separates two gas spaces. Therefore, one subsurface of the membrane exhibits predominant proton transport, while another one features mixed ionic-electronic transport.

170 Therefore, the resulting (or average) ionic transference numbers, $t_{i,av}$, should be much higher than t_i.
171 The exact $t_{i,av}$ values under OCV conditions can be calculated as follows [34]:

$$t_{i,av} = 1 - \frac{R_O}{R_O + R_p}\left(1 - \frac{E_{meas}}{E}\right), \tag{1}$$

172 where, R_O and R_p are the ohmic and polarization resistances of the PCC, while E_{meas} and E are the
173 measured and theoretically predicted potentials. As can be seen, this equation includes the
174 parameters related to the resistances of the functional materials, which can be separated using the
175 impedance spectroscopy method. The separation procedure will be described in Section 3.4 and the
176 calculation of $t_{i,av}$ values shown in Section 3.6.
177   The PCC yields such high maximal power densities (P_{max}) as 305, 360, 395 and 430 mW cm^{-2} at
178 600, 650, 700 and 750 °C, respectively (Figure 4b,d). In electrolysis mode of operation, the maximal
179 current densities reach about 640, 780, 950 and 1070 mA cm^{-2} (U = 1.5 V) at the corresponding
180 temperatures and about 295, 405, 535 and 690 mA cm^{-2} under conditions close to the thermoneutral
181 mode ($U_{TN} \approx 1.3$ V, Figure 4c,d). This mode is determined by the thermodynamic parameter of the
182 resulting reaction occurring in the rPCC (equations (2) and (3)) and corresponds to the conditions
183 when the cell is in thermal equilibrium. More precisely, the rPCC consumes heat when the bias is
184 lower than U_{TN} and, conversely, produces heat when the bias exceeds U_{TN}.

$$H_2 + 1/2O_2 \rightleftarrows H_2O, \tag{2}$$

$$U_{TN} = \frac{-\Delta H}{zF}. \tag{3}$$

185   Here, ΔH is the molar enthalpy of reaction (2), z is the number of participating electrons (z = 2)
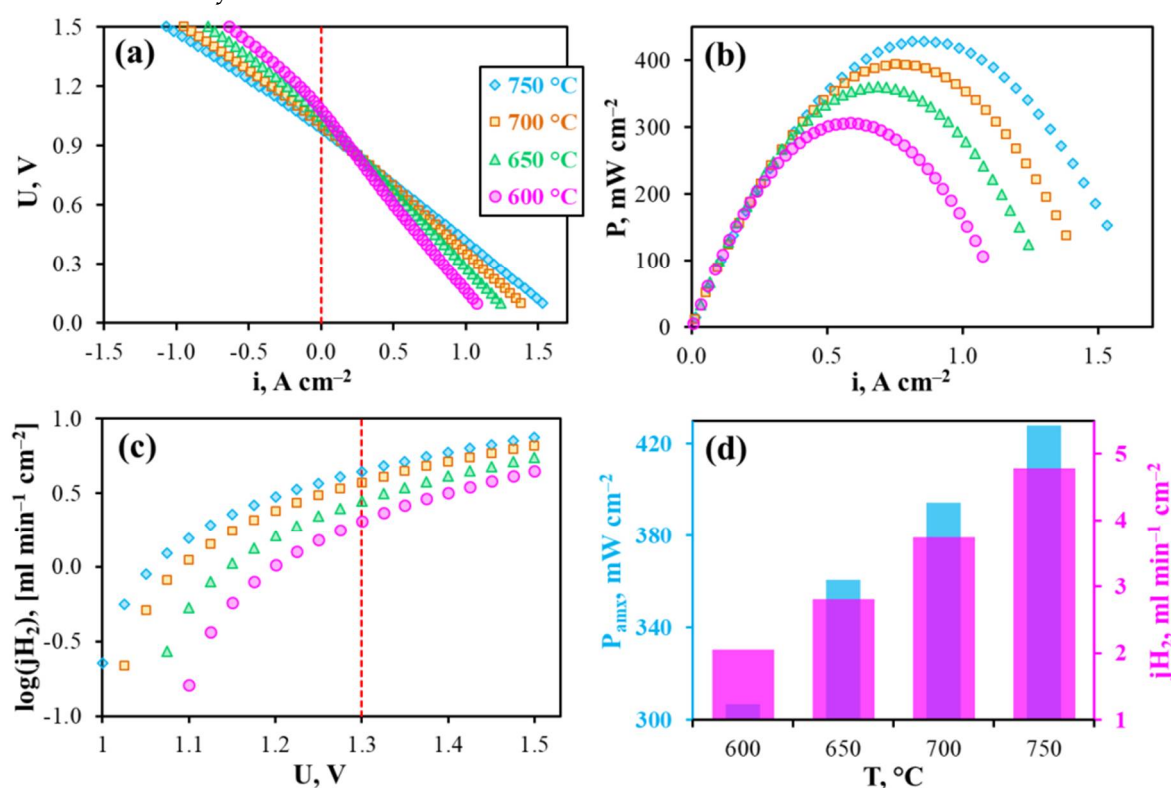186 and F is the Faraday constant.

Figure 4. Reversible operation of the PCC at different temperatures under 3%H$_2$O/H$_2$–3%H$_2$O/air conditions: volt-ampere curves (**a**), power density characteristics (**b**), maximal achievable hydrogen flux density (**c**), maximal power density and hydrogen flux density at U = 1.3 V depending on temperature (**d**).

191   *3.4. Impedance Data and Their Analysis*

192   First, the PCC's functionality was characterized under OCV mode using EIS analysis (Figure 5).
193   As can been seen from these data, all the obtained impedance spectra consist of two clearly separated
194   arcs, corresponding to low- and high-frequency processes. In order to correlate these partial processes
195   with the corresponding resistances, the experimental results were fitted by the model lines originated
196   from the used $L-R_O-(R_1Q_1)-(R_2Q_2)$ equivalent circuit scheme. Here, L is the inductance associated
197   with cables, wires and their junctions, R_O is the ohmic resistance of the electrolyte membrane, R_1 and
198   R_2 are the resistances of low- (I) and high- (II) processes, Q_1 and Q_2 are the corresponding constant
199   phase elements. Two fitting results (presented in Figure 5 as examples) confirm a good agreement
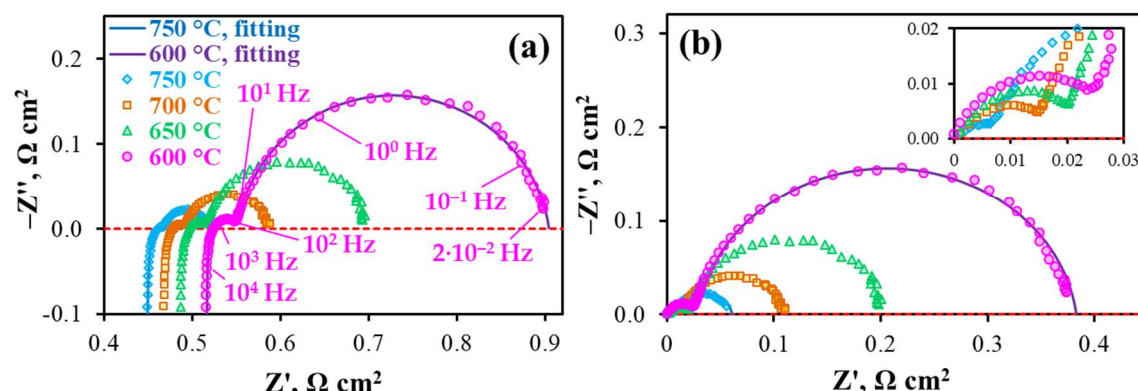200   between experimental and model data, implying the success of the used scheme.

201   **Figure 5.** Impedance spectra of the PCC at different temperatures under $3\%H_2O/H_2-3\%H_2O/air$
202   and OCV conditions: original spectra (**a**) and ones obtained after subtracting the ohmic resistance (**b**).
203

204   According to the fitting procedure, the R_O, R_1, R_2 parameters, along with the polarization
205   resistance of the electrodes ($R_p = R_1 + R_2$) and total resistance of the PCC ($R_{total} = R_O + R_p$), were
206   successfully determined, as shown in Figure 6. With increasing temperature, the total polarization
207   resistance of the PCC decreases from 0.90 to 0.52 Ω cm^2 (Figure 6a); at the same time, this resistance
208   is determined by the ohmic component (Figure 6b), the contribution of which varies between 57 and
209   86%. Two factors contribute to this result: the rather high thickness of the electrolyte used (25 μm)
210   and the excellent electrochemical properties of the electrodes, despite their fairly low porosity. The
211   total polarization resistance of the electrodes decreases from 0.39 Ω cm^2 at 600 °C to 0.07 Ω cm^2 at
212   750 °C and is regulated by the R_2 level, which contribution amounts to 91% and 71%, respectively.
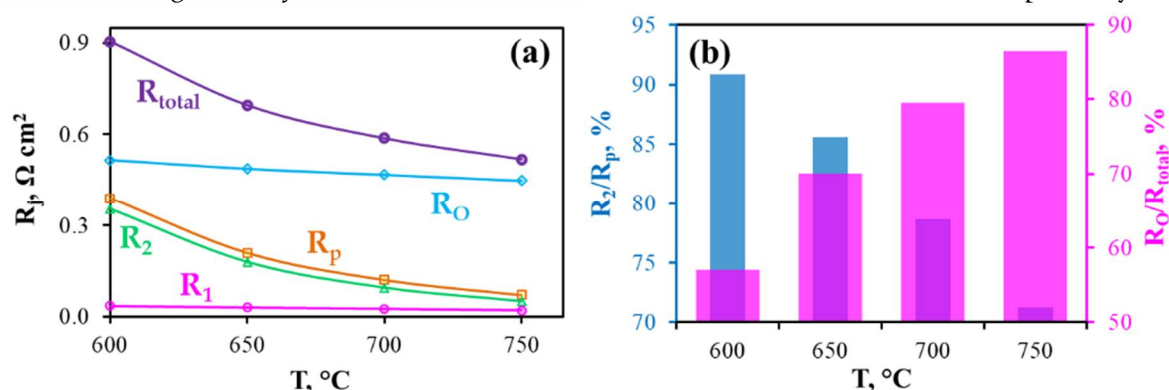

213   **Figure 6.** (**a**) Constituent resistances (R_j) of the total resistance of the PCC depending on
214   temperature; (**b**) Contributions of Process II in the total polarization resistance and the ohmic
215   resistance in the total resistance of the PCC at different temperatures.
216

217   All the constituent resistances have a thermo-activated nature with different activation energies,
218   E_a (see Appendix A, Figure A1). The Process II exhibits the highest E_a value, indicating a strong
219   correlation with temperature; conversely, the E_a level of Process I is lower than that of Process II by
220   ~3 times. The E_a level of the PCC's total resistance is quite low (0.37 eV), since it is regulated by the

221 predominant influence of the ohmic resistance with the lowest E_a. Two important conclusions are
222 supported by the obtained data:
223   (1) The low E_a for the ohmic resistance is an indirect evidence of proton behavior, since protons
224 migrate much easily than massive oxygen-ions [35,36];
225   (2) The slight temperature behavior of the total resistance of the PCC is a characteristic feature
226 of the cells, corresponding to the condition of $R_P < R_O$. Therefore, their output parameters (as shown
227 in Figure 4d) also change slightly with temperature variation.
228   In order to evaluate the prospect of utilizing the $Pr_2NiO_{4+\delta}$-based material as symmetrical
229 electrodes, Processes I and II were thoroughly analyzed by calculating the capacitance/frequency
230 values and utilizing the DRT method.
231   The values for the capacitance and frequency characteristics (at the top of the arcs) were
232 estimated from the impedance spectra fitting as follows:

$$C_j = \left(R_j \cdot Q_j \right)^{1/n_j} \cdot R_j^{-1}, \tag{4}$$

$$f_j = \left(R_j \cdot Q_j \right)^{-1/n_j} \cdot \left(2\pi \right)^{-1}, \tag{5}$$

233 where $j = 1$ or 2, n_j is the exponent factor [37,38].
234   Process I semicircles are characterized by the characteristic capacitances of $3.6 \cdot 10^{-3}$–$6.4 \cdot 10^{-3}$ F cm^{-2}
235 and characteristic frequencies of $4 \cdot 10^2$–$6 \cdot 10^2$ Hz; these values reach $8.5 \cdot 10^{-1}$–$9.0 \cdot 10^{-1}$ F cm^{-2} and $4 \cdot 10^{-1}$
236 –$4 \cdot 10^1$ Hz, respectively, for the semicircles of Process II. These results are also supported by the DRT
237 data (Figure 7). As can be seen, Processes I and II correspond to the medium- and low-frequency
238 stages, respectively. In detail, the first rate-determining step can be attributed either to the surface
239 charge-transfer phenomenon [39] or to ionic diffusion at the electrode [40] with direct participation
240 of proton charge carriers due to having a low E_a value (Figure A1). Although low values are achieved
241 for this stage at the estimated frequencies, it should be noted that the electrodes (at least, the oxygen
242 one) represent quite a dense structure for an electrolytic component, which might provide proton
243 transportation. Due to high E_a and C_2 values, the second rate-determining (and dominating) step
244 corresponds to sluggish gas-diffusion and adsorption of electrochemically-active components [41,42],
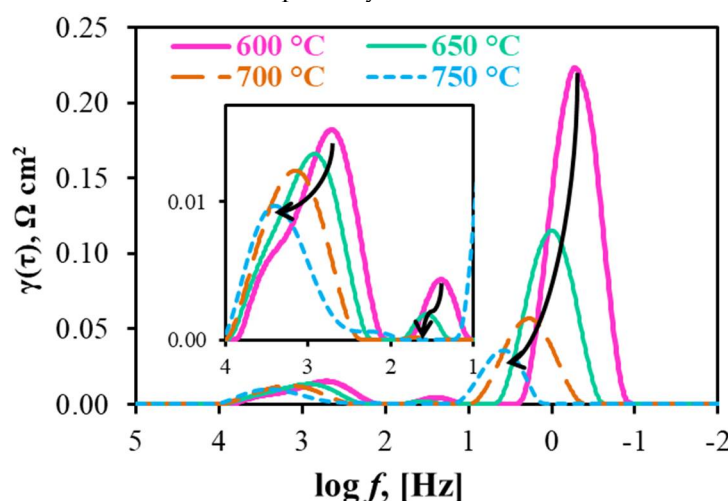245 which correlates with the mentioned low porosity of the electrodes.

246   **Figure 7.** DRT results for the obtained impedance spectra (see details in Figure 5a).
247
248   Along with these two steps, the high-resolution DRT method [43,44] gives an additional peak
249 around tens of Hz (see inset in Figure 7). The partial polarization resistance corresponding to this
250 peak (R1') does not exceed 0.005 and 0.002 Ω cm^2 (below 1.5% of R_P) at 600 and 650 °C, respectively;
251 therefore, it cannot be resolved under convenient impedance data analysis by equivalent circuits.
252 Considering its mediate frequencies and strong dependence on temperature, such a peak can likely
253 be associated with the dissociation of adsorbed molecules [41,42].

254   Summarizing, the symmetrically-formed electrodes yield a promising performance of the PCC
255 regardless of their low-porous microstructure. Moreover, the obtained results are in line with
256 characteristics for similar PCC electrolyte and oxygen electrode materials (Table 1, [45–48]).
257
258   **Table 1.** Polarization behavior of the $Pr_2NiO_{4+\delta}$-based electrodes of PCCs under OCV mode of
259   operation [1]: T is the temperature, R_P is the total polarization of the electrodes.

Electrolyte	Electrode	T, °C	R_P, Ω cm²	Ref.
$BaCe_{0.5}Zr_{0.3}Dy_{0.2}O_{3-\delta}$ (BCZD)	$Pr_{1.9}Ba_{0.1}NiO_{4+\delta}$–BCZD	600	0.39	This work
		700	0.12	
$BaCe_{0.7}Zr_{0.1}Y_{0.2}O_{3-\delta}$ (BCZY1)	$Pr_{1.8}Sr_{0.2}NiO_{4+\delta}$	600	2.17	[45]
		700	0.33	
$BaCe_{0.6}Zr_{0.2}Y_{0.2}O_{3-\delta}$ (BCZY2)	$Pr_2NiO_{4+\delta}$–BCZY2	600	0.21	[46]
		700	0.06	
BCZY1	$(Pr_{0.9}La_{0.1})_2Ni_{0.74}Cu_{0.21}Nb_{0.05}O_{4+\delta}$–BCZY1 (infiltration)	600	0.32	[47]
		700	0.13	
$BaCe_{0.9}Y_{0.1}O_{3-\delta}$	$Pr_2NiO_{4+\delta}$	600	0.80	[48]

260   [1] Polarization resistance of the Ni-cermets is assumed to be much lower than that of $Pr_2NiO_{4+\delta}$-based
261   electrodes.

3.5. Effect of Air and Hydrogen Humidification

263   It is well-known that water vapor partial pressure is a parameter determining proton transport
264 in proton-conducting electrolyte membranes [49]. From the viewpoint of the bulk structure of such
265 membranes, humidification of both atmospheres is favorable, since it results in a decrease both of
266 oxygen vacancies and hole concentrations:

$$V_O^{\bullet\bullet} + O_O^x + H_2O \rightleftarrows 2OH_O^{\bullet}, \tag{6}$$

$$V_O^{\bullet\bullet} + 1/2O_2 \rightleftarrows 2h^{\bullet} + O_O^x, \tag{7}$$

267   and, correspondingly, improved proton transport. At the same time, air humidification is considered
268 to be a more effective and easy way of suppressing some of the undesirable electronic conductivity
269 of cerates and zirconates [50,51].
270   From the perspective of thermodynamic features, the maximal achievable electrical potential
271 difference of a PCC (E or OCV) decreases with gas humidification, which follows from the
272 corresponding decrease in partial pressure gradients [52,53]:

$$E = t_{i,av} \frac{RT}{4F} \ln\left(\frac{p'O_2}{p''O_2}\right) + t_{H,av} \frac{RT}{2F} \ln\left(\frac{p''H_2O}{p'H_2O}\right) = t_{i,av}E_O + t_{H,av}E_{H_2O}, \tag{8}$$

273   where $p'O_2$ and $p''O_2$ are the oxygen partial pressures in reducing and oxidizing atmospheres, $p'H_2O$,
274 $p''H_2O$ are the water vapor partial pressures, E_O and E_{H_2O} are the electrical potential differences of
275 oxygen- and steam-concentration cells, $t_{H,av}$ is the average proton transference number. Such a
276 decrease negatively affects the performance of the cells operated in fuel mode because, in order to
277 obtain high power densities, high OCVs are necessary [54]:

$$P_{max} = \frac{E^2}{4R_{total}}. \tag{9}$$

278   Conversely, the lowest possible OCVs are needed for cells operated in electrolysis mode if these
279 OCVs are not associated with significant electron transport of the electrolytes or imperfect system
280 gas-tightness. In detail, a current density will be higher at a certain voltage value (U), while a
281 difference of U—E will be higher (or E will be lower).

282   In order to check the pH_2O effect, both atmospheres were consequentially humidified: first, air
283 atmosphere and then hydrogen atmosphere. Moreover, this allows the response of each electrode to
284 be revealed and even their contributions to the total polarization resistance, R_P, to be estimated.
285   Figure 8 shows the main electrochemical characteristics of the PCC obtained under isothermal
286 conditions with gradual increase of pH_2O. As can be seen from these data, the OCVs drop from 0.979
287 to 0.899 V, the maximal power density decreases from 430 to 290 mW cm^{-2}, while the maximal
288 achievable hydrogen flux density increases from 4.4 to 5.1 ml min^{-1} cm^{-2}, respectively, when $p''H_2O$
289 increases from 0.03 to 0.5 atm. This is in complete agreement with the abovementioned
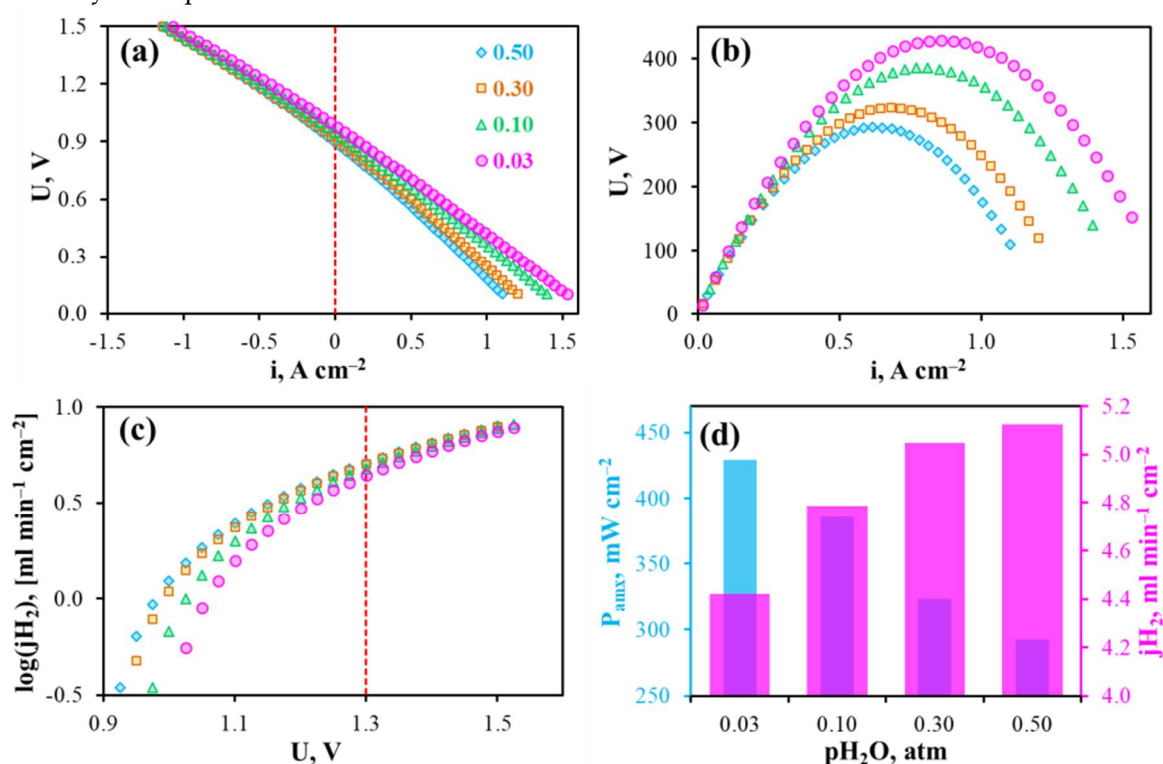290 thermodynamic predictions.

291   **Figure 8.** Reversible operation of the PCC at 750 °C depending on different pH_2O in wet air with
292 the constant fuel gas composition (3%H_2O/H_2): volt-ampere curves (**a**), power density characteristics
293 (**b**), maximal achievable hydrogen flux density (**c**), maximal power density and hydrogen flux density
294 at U = 1.3 V depending on temperature (**d**).
295
296   EIS and DRT analyses were further utilized to reveal the main tendencies in R_o and R_P changes
297 and their effects on the PCC's performance.
298   Air humidification does not change virtually the spectra's shape (Figure A2); they as well as the
299 original spectra can accurately be described by an equivalent circuit scheme with two RQ-elements.
300 On the base of DRT data (Figure A3), the distribution function consists of three well-separated peaks
301 at high $p''H_2O$ values, two of which merge at lower $p''H_2O$ values. The total polarization resistance
302 of the electrodes amounts 0.07, 0.08, 0.10 and 0.12 Ω cm^2 at 0.03, 0.10, 0.30 and 0.50 atm of $p''H_2O$. At
303 the same time, the partial resistance components vary differently (Figure A4):
304   (1) The absolute value of R1 is equal to 0.02 Ω cm^2, but its contribution as part of R_P decreases
305 from 30 to 17%;
306   (2) The contribution of R1' in R_P does not exceed 4.5% or 0.004 Ω cm^2 in absolute units;
307   (3) The contribution of R_2 increases from 70 to 80%, remaining the dominant parameter in the
308 electrode performance.
309   All the mentioned components are sensitive towards air humidification. Therefore, these stages
310 are primarily associated with oxygen electrode behavior.
311   Returning to the data of Figure 8, it can be stated that performance of the PCC is regulated by
312 the electrode activity, which dominates under OCV and fuel modes of operation. When the bias

313   exceeds the OCV level, the electrode resistance drops rapidly [55]; in this case, an improvement in
314   PCC's performance is related with a lower R_0 as a result of achieving excellent proton conductivity
315   in highly humid conditions. Making a preliminary conclusion, it can be noted that the $Pr_2NiO_{4+\delta}$-
316   based electrodes operate as a classical mixed oxygen-ionic/electronic conductor with no evidence of
317   proton transportation revealed in previously published works [46,56]. However, this might be
318   explained by the relatively high measured temperature (750 °C) leading to the insignificant water
319   uptake capability of nickelates.
320   Finally, the PCC was tested depending on temperature under $50\%H_2O/H_2 - 50\%H_2O/air$
321   conditions, corresponding to both highly-moisturized gases (Figure 9). As listed in Table A1, further
322   hydrogen humidification from 0.03 to 0.5 atm has little effect on both maximal power density
323   (decreases by ~3%) and the hydrogen evolution rate (increases by ~6%). Therefore, differences in
324   output parameters obtained at $p'H_2O = p''H_2O = 0.03$ atm (condition 1) and $p'H_2O = p''H_2O = 0.5$ atm
325   (condition 2) are mainly attributed with the pH_2O variation in air atmosphere. Such differences
326   amount to –37% of P_{max} and +13% of jH_2 at the same comparison temperature as shown in Figure 9d.
327   The obtained data are also in agreement with thermodynamic predictions, in particular with OCVs,
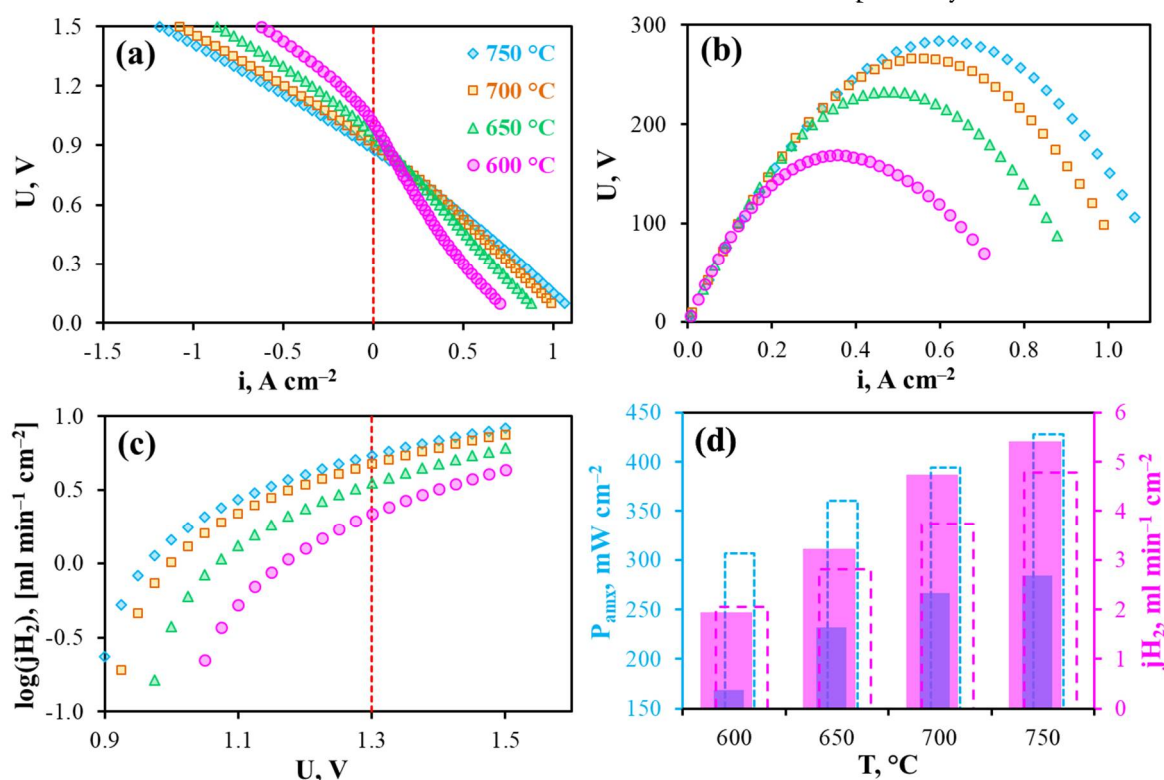328   which reach 0.991, 0.951, 0.912 and 0.874 V at 600, 650, 700 and 750 °C, respectively.

329   **Figure 9.** Reversible operation of the PCC at different temperatures under $50\%H_2O/H_2 -$
330   $50\%H_2O/air$ conditions: volt-ampere curves (**a**), power density characteristics (**b**), maximal achievable
331   hydrogen flux density (**c**), maximal power density and hydrogen flux density at U = 1.3 V depending
332   on temperature compared with those (dashed columns) obtained under $3\%H_2O/H_2 - 3\%H_2O/air$
333   conditions (**d**).

335   With increasing pH_2O in hydrogen atmosphere, the impedance spectra cannot be described by
336   the used equivalent circuit schemes, implying the appearance of additional rate-determining steps.
337   These steps might be attributed either to fuel electrode processes or even to those taking place at the
338   oxygen electrode. The latter is realized due to the fact that a change in a potential-determined
339   parameter from the one side of an electrolyte membrane results in a redistribution of the overall
340   potential and internal (ionic and electronic) currents, which can in turn affect the electrode process at
341   the other side of the same membrane. As indicated in Figure A5, hydrogen humidification (when the
342   oxidizing composition is unchanged) leads to the formation of a new distribution function, consisting
343   in different number of peaks, as well as their intensity and displacement. Such a distribution function

344 becomes more complicated with decreasing temperature (Figure 10): here, at least five independent
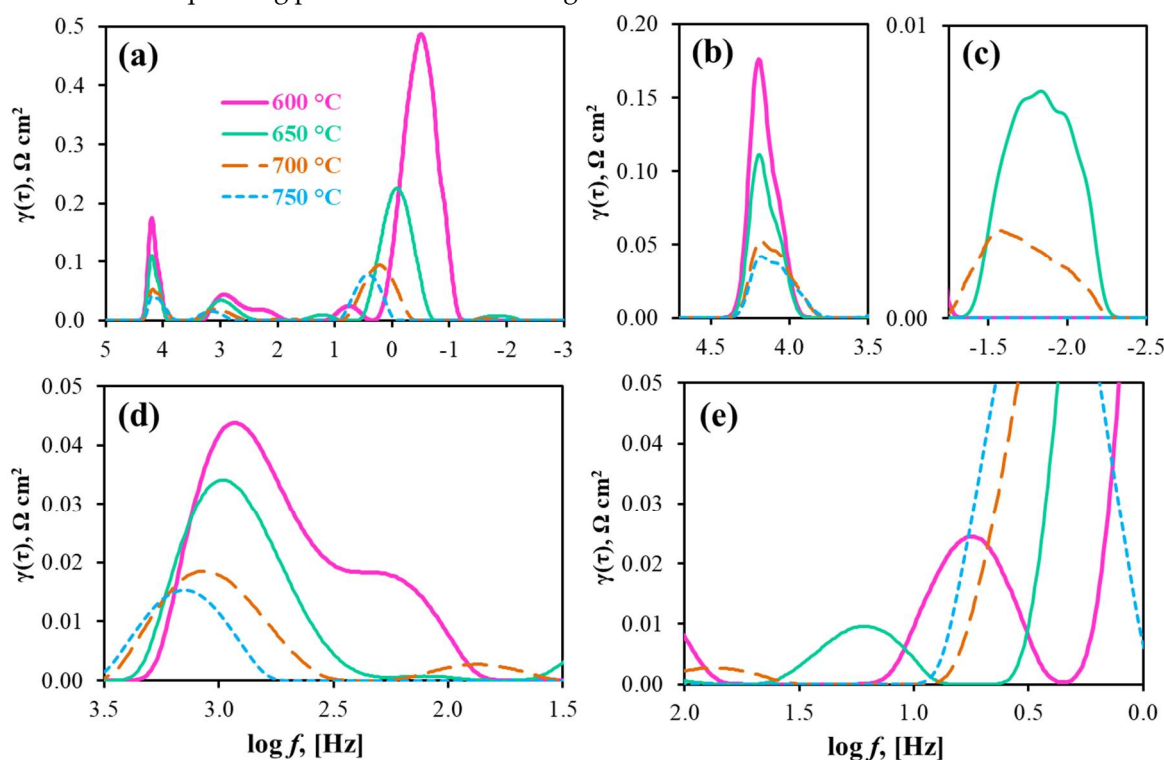345 peaks and corresponding processes can be distinguished.

Figure 10. DRT results for the impedance spectra measured for the PCC at different temperatures under $50\%H_2O/H_2$—$50\%H_2O/air$ and OCV conditions: general view (**a**) and its parts at different magnifications (**b**)–(**e**).

350 Due to the already mentioned peculiarities, the R_O values were determined as a high-frequency
351 intercept of spectra with the x-axis, while the R_P values were separately estimated as the total area
352 bounded by a $\gamma(\tau)$ function. For $50\%H_2O/H_2$—$50\%H_2O/air$ and OCV conditions, R_O is equal to 0.51,
353 0.48, 0.45 and 0.42 Ω cm², whereas R_P is equal to 0.99, 0.46, 0.21 and 0.14 Ω cm² at 600, 650, 700 and
354 750 °C, respectively. Comparing $50\%H_2O/H_2$—$50\%H_2O/air$ and $3\%H_2O/H_2$—$50\%H_2O/air$ conditions
355 at 750 °C, the R_O parameter is virtually unchanged, showing the possibility of full hydration of the
356 proton-conducting electrolyte. At the same time, R_P increases from 0.12 to 0.14 Ω cm². Such an
357 increment of R_P reaches 0.99 Ω cm² at 600 °C and 0.21 Ω cm² at 700 °C for $50\%H_2O/H_2$—$50\%H_2O/air$
358 conditions as against 0.39 Ω cm² at 600 °C and 0.12 Ω cm² at 700 °C for $3\%H_2O/H_2$—$3\%H_2O/air$
359 conditions. Therefore, not only air humidification, but also hydrogen moisturization leads to higher
360 R_P values and correspondingly lower performance characteristics. It should be noted that neither R_O
361 nor R_P indicates the efficiency of the PCC, which can, however, be estimated on the basis of the
362 electrolytic domain boundaries (absolute level and contribution of ionic conductivity).

3.6. Electrolytic Properties of the BCZD Membrane

364 In order to estimate the electrolytic properties of BCZD, which determines rPCCs' efficiency [57–
365 59], the $t_{i,av}$ values were calculated (equation (1)) using data on R_O and R_P. According to Figure 11, the
366 ionic transference numbers decrease naturally with increasing temperature due to an increase in the
367 hole conductivity contribution. Nevertheless, the $t_{i,av}$ parameter achieves quite a high level (0.90 at
368 750 °C) and, at the same time, can be further increased (up to 0.95 at the same temperature) via
369 humidification of both gases. As a result of high saturation, oxygen vacancies are almost fully filled
370 with steam, leading to a higher concentration of proton charge carriers (equation (6)) and inhibition
371 of hole charge carrier formation due to the lower concentration of free oxygen vacancies
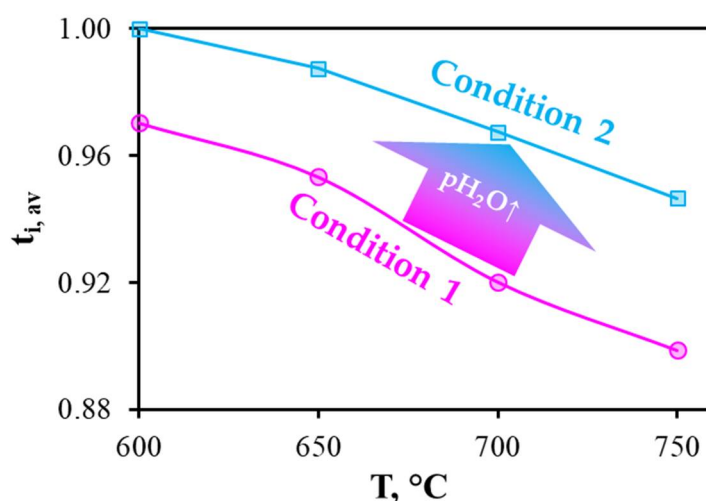372 (equation (7)).

Figure 11. Temperature dependences of the average ionic transference numbers of the BCZD electrolyte membrane in the current-free mode of the rPCC under condition 1 (p'H_2O = p''H_2O = 0.03 atm) and condition 2 (p'H_2O = p''H_2O = 0.5 atm).

The average ionic conductivity of the electrolyte membranes, determined as

$$\sigma_{i,av} = \frac{h}{R_O} \cdot t_{i,av},$$

(10)

should be considered as the most appropriate parameter (instead of total conductivity) related simultaneously with the performance (h/R_O) as well as the efficiency ($t_{i,av}$) of the electrochemical devices. For the present case, the average ionic conductivity of BCZD reaches 4.7 and 4.9 mS cm^{-1} at 600 and 700 °C under condition 1 and 4.9 and 5.4 mS cm^{-1}, respectively, under condition 2. These belong to a range of the highest values reached for proton-conducting electrolytes (Table 2, [32,47,60–74]), which agrees with the independently measured comparison of ionic conductivities of Y- and Dy-doped Ba(Ce,Zr)O_3 [75]. The abovementioned results allow the following important conclusions to be formulated:

(1) The BCZD electrolyte forms the basis for the design of novel electrochemical cells with improved output parameters due to its higher ionic conductivity compared with those for the most-studied Y-containing cerate-zirconates;

(2) Despite the negative electrochemical response of the electrodes to gas humidification, the average ionic transference and ionic conductivity values take the opposite direction, resulting in improved PCC efficiency.

392
393
394

Table 2. Electrolytic properties of proton-conducting membranes of PCCs under OCV conditions [1]: h is the thickness, T is the temperature, E is the OCV, R_O and R_P are the ohmic and polarization resistances, $t_{i,av}$ is the average ionic transference number, σ_{av} and $\sigma_{i,av}$ are the average values of total and ionic conductivities of the electrolyte membranes.

Oxygen electrode [2]	Electrolyte [3]	h, μm	T, °C	E, V	R_O, Ω cm²	R_P, Ω cm²	$t_{i,av}$	σ_{av}, mS cm⁻¹	$\sigma_{i,av}$, mS cm⁻¹	Ref.
PBN	BCZD	25	600	1.076	0.52	0.39	0.97	4.8	4.7	This work
			700	1.006	0.47	0.12	0.92	5.3	4.9	
SFM	BZCY8	1200	700	0.96	38.09	3.59	0.87	3.2	2.7	[60]
SFM	BZCY8	20	600	1.03	0.80	1.47	0.97	2.5	2.4	[61]
			700	0.96	0.57	0.33	0.91	3.5	3.2	
PLNCN	BCZY1	12	600	0.99	0.33	0.32	0.94	3.6	3.4	[47]
			700	0.95	0.21	0.13	0.91	5.8	5.2	
PBC	BCZYYC	10	600	1.00	0.37	0.34	0.94	2.7	2.5	[62]
			700	0.99	0.26	0.12	0.92	3.8	3.5	
SSC–BCZY1/	BCZY1/	9	600	1.13	0.47	0.42	1.00	1.9	1.9	[63]
			700	1.07	0.31	0.10	0.97	2.9	2.8	
GBSC	BCZY1	20	600	1.01	0.65	0.39	0.93	3.1	2.8	[64]
			700	1.02	0.52	0.08	0.92	3.8	3.6	
NBFN	BCZY1	40	600	1.11	0.84	0.71	0.99	4.8	4.7	[65]
LSCF	BCZY4	30	600	1.07	0.72	0.24	0.96	4.2	3.9	[32]
			700	1.01	0.58	0.07	0.91	5.2	4.7	
	BCZY6	30	600	1.06	0.58	0.13	0.95	5.2	4.9	
			700	0.99	0.46	0.04	0.90	6.5	5.8	
	BCZY7	30	600	1.04	1.37	0.65	0.94	2.2	2.1	
			700	0.96	0.97	0.21	0.88	3.1	2.7	

	BZY	30	600	0.93	1.34	0.82	0.89	2.2	1.9	
			700	0.84	1.13	0.29	0.80	2.7	2.1	
BSCF	BCZY1/	6	600	1.04	0.37	0.85	0.98	1.6	1.6	[66]
LSCF – BCZY3.5	BCZY3.5	8	600	1.05	0.31	1.25	0.99	2.6	2.6	[67]
			700	1.02	0.22	0.30	0.96	3.6	3.5	
LSCF – BSCZGY	BSCZGY	10	600	1.15	0.41	3.46	1.00	2.4	2.4	[68]
			700	1.13	0.19	1.82	1.00	5.4	5.4	
PBFM–SSC	BCZY1	25	600	1.01	0.41	0.54	0.95	6.1	5.8	[69]
NBFC	BCZD	30	600	1.05	0.68	0.66	0.96	4.4	4.2	[70]
			700	1.01	0.42	0.24	0.94	7.1	6.7	
NBFC′	BCZYY	25	600	1.04	1.04	0.83	0.95	2.4	2.3	[71]
			700	1.01	0.65	0.22	0.92	3.8	3.6	
PBC–BCZY	BCZY0.3	17	600	1.01	0.32	0.64	0.96	5.3	5.1	[72]
BFCC	BCZYY′	30	600	1.06	0.49	0.28	0.96	6.1	5.9	[73]
YBCZ	BCZD	20	600	1.03	0.77	0.51	0.94	2.6	2.5	[74]
			700	0.95	0.49	0.18	0.89	4.4	3.6	

395   [1] In the most cases for the listed PCCs, the gas compositions represent wet (3%H_2O) H_2 and static (or wet) air.

396   [2] Abbreviations of oxygen electrodes: PBN = $Pr_{1.9}Ba_{0.1}NiO_{4+\delta}$, SFM = $SrFe_{0.75}Mo_{0.25}O_{3-\delta}$, PLNCN = $(Pr_{0.9}La_{0.1})_2(Ni_{0.74}Cu_{0.21}Nb_{0.05})O_{4+\delta}$, PBC = $PrBaCo_2O_{5+\delta}$, SSC = $Sm_{0.5}Sr_{0.5}CoO_{3-\delta}$, GBSC =

397      $GdBa_{0.5}Sr_{0.5}Co_2O_{5+\delta}$, NBFN = $Nd_{0.5}Ba_{0.5}Fe_{0.9}Ni_{0.1}O_{3-\delta}$, LSCF = $La_{0.6}Sr_{0.4}Co_{0.2}Fe_{0.8}O_{3-\delta}$, BSCF = $Ba_{0.5}Sr_{0.5}Co_{0.8}Fe_{0.2}O_{3-\delta}$, PBFM = $(PrBa)_{0.95}(Fe_{0.9}Mo_{0.1})_2O_{5-\delta}$, NBFC = $Nd_{0.5}Ba_{0.5}Fe_{0.9}Co_{0.1}O_{3-\delta}$,

398   NBFC′ = $Nd_{0.5}Ba_{0.5}Fe_{0.9}Cu_{0.1}O_{3-\delta}$, PBC = $PrBaCo_2O_{5+\delta}$, BFCC = $BaFe_{0.6}Co_{0.3}Ce_{0.1}O_{3-\delta}$, YBCZ = $YBaCo_{3.5}Zn_{0.5}O_{7+\delta}$.

399   [3] Abbreviations of electrolytes: BCZD = $BaCe_{0.5}Zr_{0.3}Dy_{0.2}O_{3-\delta}$, BCZY1 = $BaCe_{0.7}Zr_{0.1}Y_{0.2}O_{3-\delta}$, BCZY1/ = $BaCe_{0.8}Zr_{0.1}Y_{0.1}O_{3-\delta}$, BCZY3 = $BaCe_{0.5}Zr_{0.3}Y_{0.2}O_{3-\delta}$, BCZY3.5 = $BaCe_{0.5}Zr_{0.35}Y_{0.15}O_{3-\delta}$,

400   BCZY4 = $BaZr_{0.4}Ce_{0.4}Y_{0.2}O_{3-\delta}$, BCZY6 = $BaZr_{0.6}Ce_{0.2}Y_{0.2}O_{3-\delta}$, BCZY7 = $BaZr_{0.7}Ce_{0.1}Y_{0.2}O_{3-\delta}$, BZCY8 = $BaCe_{0.1}Zr_{0.8}Y_{0.1}O_{3-\delta}$, BZY = $BaZr_{0.8}Y_{0.2}O_{3-\delta}$, BSCZGY = $Ba_{0.5}Sr_{0.5}Ce_{0.6}Zr_{0.2}Gd_{0.1}Y_{0.1}O_{3-\delta}$,

401   BCZYY = $BaCe_{0.5}Zr_{0.3}Y_{0.1}Yb_{0.1}O_{3-\delta}$, BCZYY′ = $BaCe_{0.7}Zr_{0.1}Y_{0.1}Yb_{0.1}O_{3-\delta}$, BCZYYC = $BaCe_{0.68}Zr_{0.1}Y_{0.1}Yb_{0.1}Co_{0.02}O_{3-\delta}$.

5. Conclusions

This work presents the results of fabrication and characterization of a reversible protonic ceramic cell having symmetrically-organized electrodes made of $Pr_{1.9}Ba_{0.1}NiO_{4+\delta}$ (PBN). Utilization of the same material as the functional fuel and oxygen electrode allows minimization of the thermo-chemical stress between the functional materials during high-temperature steps and even a reduction of these steps to one sintering stage, promising significant techno-economic benefits. The fabricated cell based on a 25 μm-thick $BaCe_{0.5}Zr_{0.3}Dy_{0.2}O_{3-\delta}$ (BCZD) proton-conducting electrolyte demonstrated output characteristics as high as ~300 mW cm^{-2} at 600 °C in fuel mode and ~300 mA cm^{-2} in electrolysis mode at thermoneutral conditions. The cell was tested under conditions of varying humidity in order to evaluate electrode and electrolyte performance. It was found that the PBN–BCZD oxygen electrode determined the overall electrode performance at 750 °C, operating as a dual conducting ($O^{2-}/h^\bullet$) system due to the negative electrochemical response to gas humidification. As a consequence of the high contribution of polarization resistance to the total resistance, the rPCC's performance was the same under open circuit voltage and fuel modes. On the other hand, the ohmic resistance and the average ionic transference numbers of the electrolyte membrane increased with increasing humidification, demonstrating its proton-conducting nature. Along with increased efficiency (as a result of improved electrolytic properties), the performance of the PCC was higher under humidification due to the total cell resistance being determined by the ohmic component. Although only medium performance was reached in this work (due to the rather thick electrolyte, 25 μm), the proposed strategies can effectively be used in future to resolve a number of technological issues.
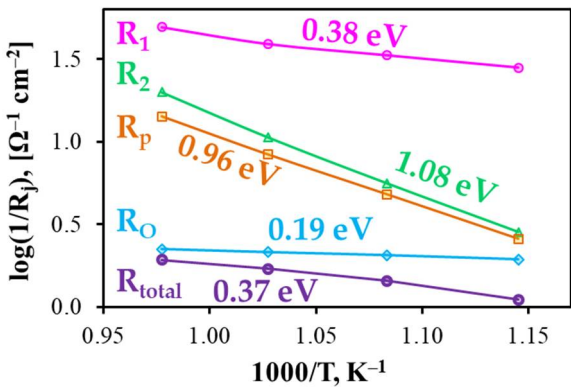
Appendix A

Figure A1. Temperature dependences of constitute resistances (R_j) of the fabricated PCC in Arrhenius coordinates. The corresponding activation energies calculated in Frenkel coordinates ($\log(T/R_j) = f(1/T)$) are also presented.
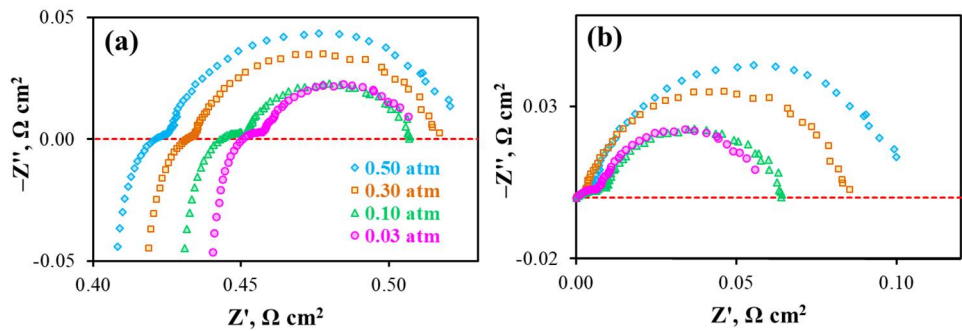
439   **Figure A2.** Impedance spectra of the PCC at 750 °C and OCV conditions depending on different
440   pH_2O in air atmosphere (fuel gas is 3%H_2O/H_2): original spectra (**a**) and those obtained after
441   subtracting the ohmic resistance (**b**)

442
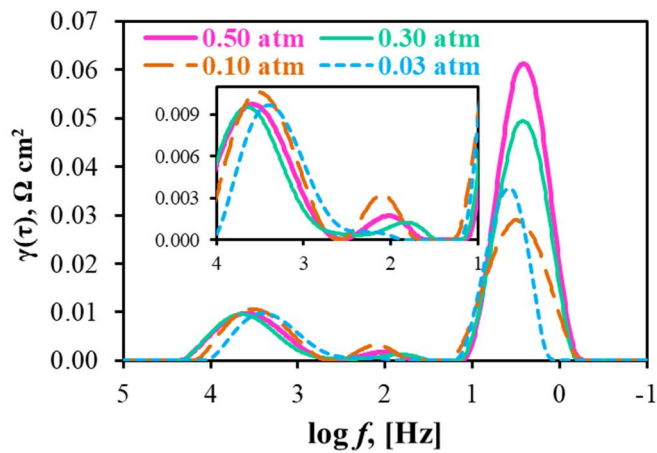
443   **Figure A3.** DRT results for the impedance spectra presented in **Figure A2**
444
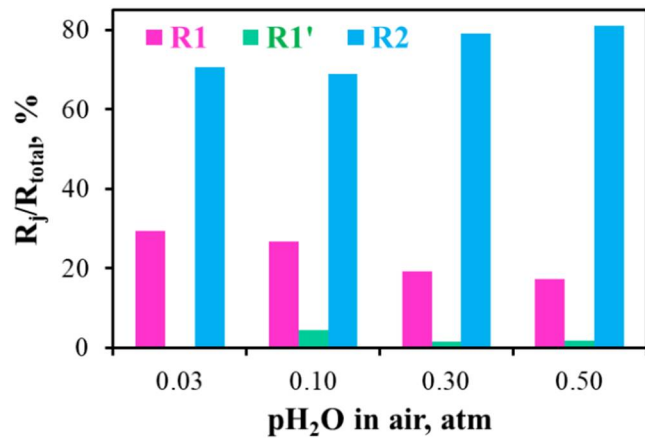
445   **Figure A4.** Contribution of partial resistances in the total resistance of the electrodes (R_P). These
446   data were obtained from the DRT results (**Figure A3**).

447
448   **Table A1.** Effect of hydrogen humidification on the PCC performance at 700 °C, when
449    $p''H_2O = 0.50$ atm. R_O and R_P are presented for OCV mode, while jH_2 is presented at U = 1.3 V.

$p'H_2O$, atm	R_O, Ω cm²	R_P, Ω cm²	P_{max}, mW cm⁻²	jH_2, ml min⁻¹ cm⁻²
0.03	0.47	0.12	293	5.1
0.50	0.45	0.21	284	5.6

450

Figure A5. DRT results for the impedance spectra measured for the PCC at 750 °C under OCV conditions at different pH_2O values in hydrogen atmosphere ($p"H_2O$ in air is equal 0.5 atm).

References

1. Medvedev, D., Murashkina, A., Pikalova, E., Demin, A., Podias, A., Tsiakaras, P. $BaCeO_3$: Materials development, properties and application. *Prog. Mater. Sci.* **2014**, *60*, 72–129, http://dx.doi.org/10.1016/j.pmatsci.2013.08.001.

2. Bi, L., Boulfrada, S., Traversa, E. Steam electrolysis by solid oxide electrolysis cells (SOECs) with proton-conducting oxides. *Chem. Soc. Rev.* **2014**, *43(24)*, 8255–8270, https://doi.org/10.1039/C4CS00194J.

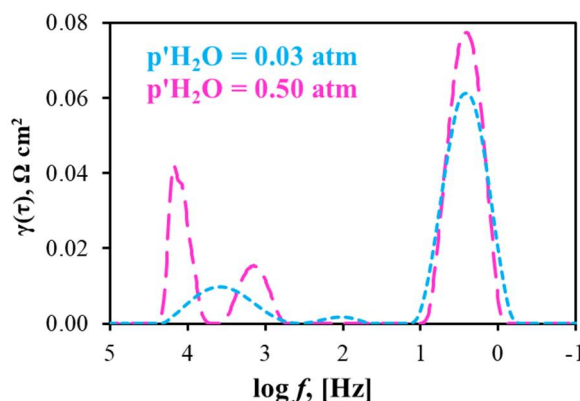3. Choi, S.M., An, H., Yoon, K.J., Kim, B.-K., Lee, H.-W., Son, J.-W., Kim, H., Shin, D., Ji, H.-L. Electrochemical analysis of high-performance protonic ceramic fuel cells based on a columnar-structured thin electrolyte. *Appl. Energy* **2019**, *233–234*, 29–36, https://doi.org/10.1016/j.apenergy.2018.10.043.

4. Mohato, N., Banerjee, A., Gupta, A., Omar, S., Balani, K. Progress in material selection for solid oxide fuel cell technology: A review. *Prog. Mater. Sci.* **2015**, *72*, 141–337, https://doi.org/10.1016/j.pmatsci.2015.01.001.

5. Gómez, S.Y., Hotza, D. Current developments in reversible solid oxide fuel cells. *Renew. Sust. Energ. Rev.* **2016**, *61*, 155–174, https://doi.org/10.1016/j.rser.2016.03.005.

6. Choi, S., Kucharczyk, C.J., Liang, Y., Zhang, X., Takeuchi, I., Ji, H.-I., Haile, S.M. Exceptional power density and stability at intermediate temperatures in protonic ceramic fuel cells. *Nat. Energy* **2018**, *3(3)*, 202–210, https://doi.org/10.1038/s41560-017-0085-9.

7. Bae, K., Jang, D.Y., Choi, H.J., Kim, D., Hong, J., Kim, B.-K., Lee, J.-H., Son, J.-W., Shim, J.H. Demonstrating the potential of yttrium-doped barium zirconate electrolyte for high-performance fuel cells. *Nat. Commun.* **2017**, *8*, 14553, https://doi.org/10.1038/ncomms14553.

8. Duan, C., Tong, J., Shang, M., Nikodemski, S., Sanders, M., Ricote, S., Almansoori, A., O'Hayre, R. Readily processed protonic ceramic fuel cells with high performance at low temperatures. *Science* **2015**, *349(6254)*, 1321–1326, http://dx.doi.org/10.1126/science.aab3987.

9. Shim, J.H. Ceramics breakthrough. *Nat. Energy* **2018**, *3(3)*, 168–169, https://doi.org/10.1038/s41560-018-0110-7.

10. Ding, D., Li, X., Lai, S.Y., Gerdes, K., Liu, M. Enhancing SOFC cathode performance by surface modification through infiltration. *Energy Environ. Sci.* **2014**, *7(2)*, 552–575, https://doi.org/10.1039/C3EE42926A.

11. Zheng, Y., Wang, J., Yu, B., Zhang, W., Chen, J., Qiao, j., Zhang, J. A review of high temperature co-electrolysis of H_2O and CO_2 to produce sustainable fuels using solid oxide electrolysis cells (SOECs): advanced materials and technology. *Chem. Soc. Rev.*, **2017**, *46(5)*, 1427-1463 https://doi.org/10.1039/C6CS00403B.

12. Su, C., Wang, W., Liu, M., Tadé, M. O., Shao, Z. Progress and Prospects in Symmetrical Solid Oxide Fuel Cells with Two Identical Electrodes. *Adv. Energy Mater.* **2015**, *5(14)*, 1500188, http://dx.doi.org/10.1002/aenm.201500188.

13. Choi, S., Sengodan, S., Park, S., Ju, Y.-W., Kim, J., Hyodo, J., Jeong, H.Y., Ishihara, T., Shin. J., Kim, G. A robust symmetrical electrode with layered perovskite structure for direct hydrocarbon solid oxide fuel cells: $PrBa_{0.8}Ca_{0.2}Mn_2O_{5+\delta}$. *J. Mater. Chem. A* **2016**, *4(5)*, 1747–1753, https://doi.org/10.1039/C5TA08878J.

14. Shen, J., Chen, Y., Yang, G., Zhou, W., Tadé, M. O., Shao, Z. Impregnated $LaCo_{0.3}Fe_{0.67}Pd_{0.03}O_{3-\delta}$ as a promising electrocatalyst for "symmetrical" intermediate-temperature solid oxide fuel cells. *J. Power Sources* **2016**, *306*, 92–99, https://doi.org/10.1016/j.jpowsour.2015.12.021.

15. Tao, H., Xie, J., Wu, Y., Wang, S. Evaluation of $PrNi_{0.4}Fe_{0.6}O_{3-\delta}$ as a symmetrical SOFC electrode material. *Int. J. Hydrogen Energy* **2018**, *43(32)*, 15423–15432, https://doi.org/10.1016/j.ijhydene.2018.06.047.

16. Niu, B., Jin, F., Zhang, L., Shen, P., He, T. Performance of double perovskite symmetrical electrode materials $Sr_2TiFe_{1-x}Mo_xO_{6-\delta}$ (x = 0.1, 0.2) for solid oxide fuel cells. *Electrochim. Acta* **2018**, *263*, 217–227, https://doi.org/10.1016/j.electacta.2018.01.062.

17. Lan, R., Cowin, P. I., Sengodan, S., Tao, S. A perovskite oxide with high conductivities in both air and reducing atmosphere for use as electrode for solid oxide fuel cells. *Sci. Rep.* **2016**, *6(1)*, https://doi.org/10.1038/srep31839.

18. Gao, Z., Ding, X., Ding, D., Ding, L., Zhang, S., Yuan, G. Infiltrated Pr_2NiO_4 as promising bi-electrode for symmetrical solid oxide fuel cells. *Int. J. Hydrogen Energy* **2018**, *43(18)*, 8953–8961, https://doi.org/10.1016/j.ijhydene.2018.03.164.

19. Nicollet, C., Flura, A., Vibhu, V., Rougier, A., Bassat, J.-M., Grenier, J.-C. An innovative efficient oxygen electrode for SOFC: Pr_6O_{11} infiltrated into Gd-doped ceria backbone. *Int. J. Hydrogen Energy* **2016**, *41(34)*, 15538–15544, https://doi.org/10.1016/j.ijhydene.2016.04.024.

20. Lyagaeva, J., Medvedev, D., Pikalova, E., Plaksin, S., Brouzgou, A., Demin, A., Tsiakaras, P. A detailed analysis of thermal and chemical compatibility of cathode materials suitable for $BaCe_{0.8}Y_{0.2}O_{3-\delta}$ and $BaZr_{0.8}Y_{0.2}O_{3-\delta}$ proton electrolytes for solid oxide fuel cell application. *Int. J. Hydrogen Energy* **2017**, *42(3)*, 1715–1723, http://dx.doi.org/10.1016/j.ijhydene.2016.07.248.

21. Pikalova, E., Kolchugin, A., Bogdanovich, N., Medvedev, D., Lyagaeva, J., Vedmid', L., Anayev, M., Plaksin, S., Farlenkov, A., Suitability of $Pr_{2-x}Ca_xNiO_{4+\delta}$ as cathode materials for electrochemical devices based on oxygen ion and proton conducting solid state electrolytes. *Int. J. Hydrogen Energy* **2018**, [in press], https://doi.org/10.1016/j.ijhydene.2018.06.023.

22. Lyagaeva, J., Danilov, N., Vdovin, G., Bu, J., Medvedev, D., Demin, A., Tsiakaras, P. A new Dy-doped $BaCeO_3$–$BaZrO_3$ proton-conducting material as a promising electrolyte for reversible solid oxide fuel cells. *J. Mater. Chem. A* **2016**, *4(40)*, 15390–15399, https://doi.org/10.1039/C6TA06414K.

23. Pikalova, E. Y., Medvedev, D. A., Khasanov, A. F. Structure, stability, and thermomechanical properties of Ca-substituted $Pr_2NiO_{4+\delta}$. *Phys. Solid State* **2017**, *59(4)*, 694–702, https://doi.org/10.1134/S1063783417040187.

24. http://www.ihte.uran.ru/?page_id=3154 (accessed on 07.11.18).

25. Pikalova, E., Kolchugin, A., Filonova, E., Bogdanovich, N., Pikalov, S., Ananyev, M., Molchanova, N., Farlenkov, A. Validation of calcium-doped neodymium nickelates as SOFC air electrode materials. *Solid State Ionics* **2018**, *319*, 130–140. https://doi.org/10.1016/j.ssi.2018.02.008.

26. Akbari-Fakhrabadi, A., Toledo, E.G., Canales, J.I., Meruane, V., Chan, S.H., Gracia-Pinilla, M.A. Effect of Sr^{2+} and Ba^{2+} doping on structural stability and mechanical properties of $La_2NiO_{4+\delta}$. *Ceram. Int.* **2018**, *44(9)*, 10551–10557. https://doi.org/10.1016/j.ceramint.2018.03.077.

27. Kravchenko, E., Khalyavin, D., Zakharchuk, K., Grins, J., Svensson, G., Pankov, V., Yaremchenko, A. High-temperature characterization of oxygen-deficient K_2NiF_4-type $Nd_{2-x}Sr_xNiO_{4-\delta}$ (x = 1.0–1.6) for potential SOFC/SOEC applications. *J. Mater. Chem. A* **2015**, *3(47)*, 23852–23863. https://doi.org/10.1039/c5ta06779k.

28. Hua B., Li M., Sun Y.-F., Li J.-H., Luo J.-L. Enhancing perovskite electrocatalysis of solid oxide cells through controlled exsolution of nanoparticles. *ChemSusChem* **2017**, *10(17)*, 3333–3341. https://doi.org/10.1002/cssc.201700936.

29. Løken, A., Ricote, S., Wachowski, S. Thermal and chemical expansion in proton ceramic electrolytes and compatible electrodes. *Crystals* **2018**, *8(9)*, 365, http://dx.doi.org/10.3390/cryst8090365.

30. Kharton, V. V., Kovalevsky, A. V., Avdeev, M., Tsipis, E. V., Patrakeev, M. V., Yaremchenko, A. A., Naumovich, E.N., Frade, J.R. Chemically induced expansion of $La_2NiO_{4+\delta}$-based materials. *Chem. Mater.* **2007**, *19(8)*, 2027–2033, http://dx.doi.org/10.1021/cm070096x.

31. Kochetova, N., Animitsa, I., Medvedev, D., Demin, A., Tsiakaras, P. Recent activity in the development of proton-conducting oxides for high-temperature applications. *RSC Adv.* **2016**, *6(77)*, 73222–73268, https://doi.org/10.1039/c6ra13347a.

32. Jeong, S., Kobayashi, T., Kuroda, K., Kwon, H., Zhu, C., Habazaki, H., Aoki, Y. Evaluation of thin film fuel cells with Zr-rich $BaZr_xCe_{0.8-x}Y_{0.2}O_{3-\delta}$ electrolytes (x ≥ 0.4) fabricated by a single-step reactive sintering method. *RSC Adv.* **2018**, *8(46)*, 26309–26317, https://doi.org/10.1039/C8RA04724C.

33. Danilov, N. A., Lyagaeva, J. G., Medvedev, D. A., Demin, A. K., Tsiakaras, P. Transport properties of highly dense proton-conducting $BaCe_{0.8-x}Zr_xDy_{0.2}O_{3-\delta}$ materials in low- and high-temperature ranges. *Electrochim. Acta* **2018**, *284*, 551–559, https://doi.org/10.1016/j.electacta.2018.07.179.

546 34. Liu, M., Hu, H. Effect of interfacial resistance on determination of transport properties of mixed-conducting
547   electrolytes.   *J. Electrochem. Soc.* **1996**, *143(6)*, L109–L112, http://dx.doi.org/10.1149/1.1836892.

548 35. Kreuer,   K.D.   Proton-conducting   oxides.   *Annu.   Rev.   Mater.   Res.*   **2003**,   *33(1)*,   333–359,
549   https://doi.org/10.1146/annurev.matsci.33.022802.091825.

550 36. Malavasi, L., Fisher, C.A. J., Islam, M.S. Oxide-ion and proton conducting electrolyte materials for clean
551   energy applications: structural and mechanistic features. *Chem. Soc. Rev.* **2010**, *39(11)*, 4370-4387,
552   https://doi.org/10.1039/B915141A.

553 37. Gregori, G., Merkle, R., Maier, J. Ion conduction and redistribution at grain boundaries in oxide systems.
554   Prog. Mater. Sci. **2017**, *89*, 252–305, http://dx.doi.org/10.1016/j.pmatsci.2017.04.009.

555 38. Nechache, A., Cassir, M., Ringuedé, A. Solid oxide electrolysis cell analysis by means of electrochemical
556   impedance   spectroscopy: A   review.   *J.   Power   Sources   **2014**,   258,   164–181,*
557   https://doi.org/10.1016/j.jpowsour.2014.01.110.

558 39. Zheng, M., Wang, S., Yang, Y. Xia, C. Barium carbonate as a synergistic catalyst for the H_2O/CO_2 reduction
559   reaction at Ni–yttria stabilized zirconia cathodes for solid oxide electrolysis cells. *J. Mater. Chem. A* **2018**,
560   *6(6)*, 2721–2729, http://dx.doi.org/10.1039/c7ta08249e.

561 40. Sun, S., Cheng, Z. Electrochemical behaviors for Ag, LSCF and BSCF as oxygen electrodes for proton
562   conducting IT-SOFC. *J. Electrochem. Soc.* **2017**, *164(10)*, F3104–F3113, http://dx.doi.org/10.1149/2.0121710jes.

563 41. Shi, N., Su, F., Huan, D., Xie, Y., Lin, J., Tan, W., Peng, R., Xia, C., Chen, C., Lu, Y. Performance and DRT
564   analysis of P-SOFCs fabricated using new phase inversion combined tape casting technology. *J. Mater.*
565   *Chem. A* **2017**, *5(37)*, 19664–19671, http://dx.doi.org/10.1039/c7ta04967f.

566 42. Wang, X., Ma, Z., Zhang, T., Kang, J., Ou, X., Feng, P., Wang, S., Zhou, F., Ling, Y. Charge transfer modeling
567   and polarization DRT analysis of proton ceramics fuel cells based on mixed conductive electrolyte with the
568   modified   anode-electrolyte   interface.   *ACS   Appl.   Mater.   Interfaces*   **2018**,   *10(41)*,   35047–35059.
569   http://dx.doi.org/10.1021/acsami.8b10429.

570 43. Boukamp, B. A. Fourier transform distribution function of relaxation times; application and limitations.
571   *Electrochim*. Acta **2015**, *154*, 35–46, https://doi.org/10.1016/j.electacta.2014.12.059.

572 44. Ivers-Tiffée, E., Weber, A. Evaluation of electrochemical impedance spectra by the distribution of relaxation
573   times. J. Ceram. Soc. Jpn. **2017**, 125(4), 193–201, https://doi.org/10.2109/jcersj2.16267.

574 45. Yang, S., Wen, Y., Zhang, J., Lu, Y., Ye, X., Wen, Z. Electrochemical performance and stability of cobalt-free
575       $Ln_{1.2}Sr_{0.8}NiO_4$ (Ln=La and Pr) air electrodes for proton-conducting reversible solid oxide cells. *Electrochim.*
576   *Acta* 2018, *267*, 269–277, https://doi.org/10.1016/j.electacta.2018.02.053.

577 46. Li, W., Guan, B., Ma, L., Hu, S., Zhang, N., Liu, X. High performing triple-conductive $Pr_2NiO_{4+\delta}$ anode for
578   proton-conducting steam solid oxide electrolysis cell**.** *J. Mater. Chem. A* **2018**, *6(37)*, 18057–18066,
579   https://doi.org/10.1039/C8TA04018D.

580 47. Li, G., Jin, H., Cui, Y., Gui, L., He, B., Zhao, L. Application of a novel $(Pr_{0.9}La_{0.1})_2(Ni_{0.74}Cu_{0.21}Nb_{0.05})O_{4+\delta}$-
581   infiltrated $BaZr_{0.1}Ce_{0.7}Y_{0.2}O_{3-\delta}$ cathode for high performance protonic ceramic fuel cells. *J. Power Sources*
582   **2017**, *341*, 192–198, https://doi.org/10.1016/j.jpowsour.2016.11.008.

583 48. Dailly, J., Marrony, M., Taillades, G., Taillades-Jacquin, M., Grimaud, A., Mauvy, F., Louradour, E., Salmi,
584   J. Evaluation of proton conducting BCY10-based anode supported cells by co-pressing method: Up-scaling,
585   performances   and   durability.   *J. Power Sources*   **2014**,   *255*,   302–307,
586   https://doi.org/10.1016/j.jpowsour.2013.12.082.

587 49. Wang, W., Medvedev, D., Shao, Z. Gas Humidification impact on the properties and performance of
588   perovskite-type functional materials in proton-conducting solid oxide cells. *Adv. Funct. Mater.* **2018**, *28(48)*,
589   1802592. https://doi.org/10.1002/adfm.201802592.

590 50. Heras-Juaristi, G., Pérez-Coll, D., Mather, G.C. Temperature dependence of partial conductivities of the
591       $BaZr_{0.7}Ce_{0.2}Y_{0.1}O_{3-\delta}$ proton   conductor.   *J. Power Sources*   **2017**,   *364*,   52–60,
592   https://doi.org/10.1016/j.jpowsour.2017.08.011.

593 51. Lyagaeva, J., Danilov, N., Korona, D., Farlenkov, A., Medvedev, D., Demin, A., Animitsa, I., Tsiakaras, P.
594   Improved ceramic and electrical properties of $CaZrO_3$-based proton-conducting materials prepared by a
595   new   convenient   combustion   synthesis   method.   *Ceram. Int.*   **2017**,   *43(9)*,   7184–7192,
596   http://dx.doi.org/10.1016/j.ceramint.2017.03.006.

597 52. Norby, T. EMF method determination of conductivity contributions from protons and other foreign ions
598   in oxides. *Solid State Ionics* **1988**, *28–30*, 1586–1591, https://doi.org/10.1016/0167-2738(88)90424-9.

599 53. Sutija, D. Transport number determination by the concentration-cell/open-circuit voltage method for
600   oxides with mixed electronic, ionic and protonic conductivity. *Solid State Ionics* **1995**, *77*, 167–174,
601   https://doi.org/10.1016/0167-2738(94)00268-W.
602 54. Gong, Z., Sun, W., Cao, J., Shan, D., Wu, Y., Liu, W. $Ce_{0.8}Sm_{0.2}O_{1.9}$ decorated with electron-blocking acceptor-
603   doped $BaCeO_3$ as electrolyte for low-temperature solid oxide fuel cells. *Electrochim. Acta* **2017**, 228, 226–232,
604   https://doi.org/10.1016/j.electacta.2017.01.065.
605 55. Huan, D., Shi, N., Zhang, L., Tan, W., Xie, Y., Wang, W., Xia, C., Lu, Y. New, Efficient, and reliable air
606   electrode material for proton-conducting reversible solid oxide cells. *ACS Appl. Mater. Interfaces* **2018**, *10(2)*,
607   1761–1770, http://dx.doi.org/10.1021/acsami.7b16703.
608 56. Philippeau, B., Mauvy, F., Mazataud, C., Fourcade, S., Grenier, J.-C. Comparative study of electrochemical
609   properties of mixed conducting $Ln_2NiO_{4+\delta}$ (Ln = La, Pr and Nd) and $La_{0.6}Sr_{0.4}Fe_{0.8}Co_{0.2}O_{3-\delta}$ as SOFC cathodes
610   associated to $Ce_{0.9}Gd_{0.1}O_{2-\delta}$, $La_{0.8}Sr_{0.2}Ga_{0.8}Mg_{0.2}O_{3-\delta}$ and $La_9Sr_1Si_6O_{26.5}$ electrolytes. *Solid State Ionics* **2013**, *249–
611   250*, 17–25, https://doi.org/10.1016/j.ssi.2013.06.009.
612 57. Nakamura, T., Mizunuma, S., Kimura, Y., Mikami, Y., Yamauchi, K., Kuroha, T., Taniguchi, N., Tsuji. Y.,
613   Okuyama, Y., Amezawa, K. Energy efficiency of ionic transport through proton conducting ceramic
614   electrolytes for energy conversion applications. *J. Mater. Chem. A* **2018**, *6(32)*, 15771–15780.
615   http://dx.doi.org/10.1039/c8ta05373a.
616 58. Ji, H.-I., Kim, H., Lee, H.-W., Kim, B.-K., Son, J.-W., Yoon, K. J., Lee, J.-H. Open-cell voltage and electrical
617   conductivity of a protonic ceramic electrolyte under two chemical potential gradients. *Phys. Chem. Chem.
618   Phys.* **2018**, *20(22)*, 14997–15001, http://dx.doi.org/10.1039/c8cp01880d.
619 59. Zhang, J.-H., Lei, L.-B., Liu, D., Zhao, F.-Y., Ni, M., Chen, F. Mathematical modeling of a proton-conducting
620   solid   oxide   fuel   cell   with   current   leakage.   *J.   Power   Sources*   **2018**,   *400*,   333–340,
621   https://doi.org/10.1016/j.jpowsour.2018.08.038.
622 60. Wachowski, S., Li, Z., Polfus, J.M., Norby, T. Performance and stability in H_2S of $SrFe_{0.75}Mo_{0.25}O_{3-\delta}$ as
623   electrode   in   proton   ceramic   fuel   cells.   *J.   Eur.   Ceram.   Soc.*   **2018**,   *38(1)*,   163–171,
624   https://doi.org/10.1016/j.jeurceramsoc.2017.08.020.
625 61. Nasani, N., Ramasamy, D., Mikhalev, S., Kovalevsky, A.V., Fagg, D.P. Fabrication and electrochemical
626   performance of a stable, anode supported thin $BaCe_{0.4}Zr_{0.4}Y_{0.2}O_{3-\delta}$ electrolyte protonic ceramic fuel cell. *J.
627   Power Sources* **2015**, *278*, 582–589, https://doi.org/10.1016/j.jpowsour.2014.12.124.
628 62. Wan, Y., He, B., Wang, R., Ling, Y., Zhao, L. Effect of Co doping on sinterability and protonic conductivity
629   of $BaZr_{0.1}Ce_{0.7}Y_{0.1}Yb_{0.1}O_{3-\delta}$ for   protonic   ceramic   fuel   cells.   *J. Power Sources*   **2017**,   *347*,   14–20,
630   https://doi.org/10.1016/j.jpowsour.2017.02.049.
631 63. Dailly,   J.,   Taillades,   G.,   Ancelin,   M.,   Pers,   P.,   Marrony,   M.   High   performing
632       $BaCe_{0.8}Zr_{0.1}Y_{0.1}O_{3-\delta}$–$Sm_{0.5}Sr_{0.5}CoO_{3-\delta}$ based protonic ceramic fuel cell. *J. Power Sources* **2017**, *361*, 221–226,
633   https://doi.org/10.1016/j.jpowsour.2017.06.089.
634 64. Ding, H., Xue, X. $GdBa_{0.5}Sr_{0.5}Co_2O_{5+\delta}$ layered perovskite as promising cathode for proton conducting solid
635   oxide fuel cells. *J Alloys Compd.* 2010, *496(1–2)*, 683–686, https://doi.org/10.1016/j.jallcom.2010.02.169.
636 65. Shi, H., Ding, Z., Ma, G. Electrochemical performance of cobalt-free $Nd_{0.5}Ba_{0.5}Fe_{1-x}Ni_xO_{3-\delta}$ cathode materials
637   for   intermediate   temperature   solid   oxide   fuel   cells.   *Fuel   Cells*   **2016**,   *16(2)*,   258–262,
638   https://doi.org/10.1002/fuce.201500156.
639 66. Dailly, J., Ancelin, M., Marrony, M. Long term testing of BCZY-based protonic ceramic fuel cell PCFC:
640   Micro-generation profile and reversible production of hydrogen and electricity. *Solid State Ionics* **2017**, 306,
641   69–75, http://dx.doi.org/10.1016/j.ssi.2017.03.002.
642 67. Lee,   S.,   Park,   S.,   Wee,   S.,   Baek,   H.,   Shin,   D.   One-dimensional   structured $La_{0.6}Sr_{0.4}Co_{0.2}Fe_{0.8}O_{3-\delta}$ -
643       $BaCe_{0.5}Zr_{0.35}Y_{0.15}O_{3-\delta}$ composite cathode for protonic ceramic fuel cells. *Solid State Ionics* **2018**, *320*, 347–352.
644   https://doi.org/10.1016/j.ssi.2018.03.010.
645 68. Amiri, T., Singh, K., Sandhu, N. K., Hanifi, A. R., Etsell, T. H., Luo, J.-L., Thangadurai, V., Sarkar, P. High
646   performance tubular solid oxide fuel cell based on $Ba_{0.5}Sr_{0.5}Ce_{0.6}Zr_{0.2}Gd_{0.1}Y_{0.1}O_{3-\delta}$ proton conducting
647   electrolyte. *J. Electrochem. Soc.* **2018**, *165*, F764–F769. http://dx.doi.org/10.1149/2.0331810jes.
648 69. Li, F., Tao, Z., Dai, H., Xi, X., Ding, H. A high-performing proton-conducting solid oxide fuel cell with
649   layered perovskite cathode in intermediate temperatures. *Int. J. Hydrogen Energy* **2018**, *43*, 19757–19762.
650   https://doi.org/10.1016/j.ijhydene.2018.09.022.

651 70. Lyagaeva, J., Danilov, N., Tarutin, A., Vdovin, G., Medvedev, D., Demin, A., Tsiakaras, P. Designing a
652   protonic ceramic fuel cell with novel electrochemically active oxygen electrodes based on doped
653      $Nd_{0.5}Ba_{0.5}FeO_{3-\delta}$. *Dalton Trans.* **2018**, *47*, 5149–8157.

654 71. Lyagaeva, J., Vdovin, G., Hakimova, L., Medvedev, D., Demin, A., Tsiakaras, P. $BaCe_{0.5}Zr_{0.3}Y_{0.2-x}Yb_xO_{3-\delta}$
655   proton-conducting electrolytes for intermediate-temperature solid oxide fuel cells. Electrochim. Acta 2017,
656   251, 554–561. http://dx.doi.org/10.1016/j.electacta.2017.08.149.

657 72. Gui, L., Ling, Y., Li, G., Wang, Z., Wan, Y., Wang, R., He, B., Zhao, L. Enhanced sinterability and
658   conductivity of $BaZr_{0.3}Ce_{0.5}Y_{0.2}O_{3-\delta}$ by addition of bismuth oxide for proton conducting solid oxide fuel cells.
659   *J. Power Sources* **2016**, *301*, 369–375. https://doi.org/10.1016/j.jpowsour.2015.10.029.

660 73. Zhang, L., Li, C. $BaFe_{0.6}Co_{0.3}Ce_{0.1}O_{3-\delta}$ as cathode materials for proton-conducting solid oxide fuel cells.
661   Ceram. Int. 2016, 42, 10511–10515. https://doi.org/10.1016/j.ceramint.2016.03.141.

662 74. Danilov, N.A., Tarutin, A.P., Lyagaeva, J.G., Pikalova, E.Yu., Murashkina, A.A., Medvedev, D.A.,
663   Patrakeev, M.V., Demin, A.K. Affinity of $YBaCo_4O_{7+\delta}$-based layered cobaltites with protonic conductors
664   of cerate-zirconate family. Ceram. Int. 2017, 43, 15418–15423. https://doi.org/10.1016/j.ceramint.2017.08.083.

665 75. Danilov, N., Pikalova, E., Lyagaeva, J., Antonov, B., Medvedev, D., Demin, A., Tsiakaras, P. Grain and grain
666   boundary transport in $BaCe_{0.5}Zr_{0.3}Ln_{0.2}O_{3-\delta}$ (Ln – Y or lanthanide) electrolytes attractive for protonic ceramic
667   fuel cells application. *J. Power Sources* **2017**, *366*, 161–168, http://dx.doi.org/10.1016/j.jpowsour.2017.09.021.